RAPID COMMUNICATION

Interparticle-friction-induced anomalous colloid structure

RAPID COMMUNICATION

Interparticle-friction-induced anomalous colloid structure

Fuzhou Liu(刘福洲)[1,2,†], Yu Ding(丁宇)[1,2], Longfei Li(黎龙飞)[1,2], Ke Cheng(程可)[1,2], Fangfu Ye(叶方富)[1,2,3,4,5,‡], and Mingcheng Yang(杨明成)[1,2,5,§]

[1] *Beijing National Laboratory for Condensed Matter Physics and CAS Key Laboratory of Soft Matter Physics, Institute of Physics, Chinese Academy of Sciences (CAS), Beijing* 100190, *China*

[2] *School of Physical Sciences, University of Chinese Academy of Sciences, Beijing* 100049, *China*

[3] *Wenzhou Institute, University of Chinese Academy of Sciences, Wenzhou* 325001, *China*

[4] *Oujiang Laboratory (Zhejiang Laboratory for Regenerative Medicine, Vision and Brain Health), Wenzhou* 325000, *China*

[5] *Songshan Lake Materials Laboratory, Dongguan* 523808, *China*

(Received 11 October 2024; revised manuscript received 4 November 2024; accepted manuscript online 15 November 2024)

Interparticle frictional interactions are ubiquitous in colloidal systems, exerting a profound influence on their structural and physical attributes. In this study, we employed Brownian dynamics simulations to explore the non-equilibrium dynamics in colloidal systems, focusing particularly on the role of tangential friction and its influence on the macroscopic physical properties of colloids. We found that the disruption of instantaneous time-reversal symmetry by tangential frictional interactions can trigger the self-assembly of colloidal systems into intricate network configurations, and these novel structures exhibit unique depletion force and rheological properties that set them apart from traditional colloidal gel systems. These findings not only help deepen our comprehension of the self-assembly phenomena in non-equilibrium colloidal systems but also offer fresh insights for the development of colloidal materials with tailored characteristics.

Keywords: colloids, networks, self-assembly, Brownian dynamics

PACS: 64.70.pv, 64.60.aq, 64.75.Yz, 83.10.Mj

DOI: 10.1088/1674-1056/ad9300 **CSTR:** 32038.14.CPB.ad9300

1. Introduction

Particle surface roughness can significantly modulate the physical properties of colloids, such as wettability, adhesion, and interfacial interactions.[1] This attribute has been ingeniously harnessed in the engineering of functional colloidal materials,[1,2] ranging from superhydrophobic interfaces,[3] to stabilization of colloidal dispersions,[4] and drug delivery.[5] The interactions among rough spherical particles are notably intricate, characterized by the complex interplay between tangential contact and normal forces.[6–8] Recent studies involving graphene monolayers and amorphous silicon have unveiled a phenomenon of load-dependent frictional hysteresis.[9–16] This phenomenon demonstrates that the magnitude of tangential friction at the interface during the compression (loading) is not equivalent to that observed during the decompression (unloading), indicating a time-reversal symmetry breaking in this type of friction, and the consequences of this time-reversal symmetry breaking on colloidal properties remain largely unknown.[17]

In general, particle surface roughness can affect the self-assembling patterns in colloidal systems, with network-like structures emerging as a particularly prevalent and intriguing configuration.[1,18–20] Network structures are ubiquitous in colloidal systems, such as colloidal gels, polymer colloids and superparamagnetic colloids driven by temporally varying magnetic fields.[21–23] In these systems, colloidal interactions are often anisotropic, or an external field may induce particle polarity. A typical example of a network structure without external driving force is colloidal gels, which can be broadly categorized into two types: chemical gels and physical gels (or thermoreversible gels).[24] In chemical gels, the crosslinks between particles are established through irreversible covalent bonding, while in physical gels interparticle connections are mediated by non-covalent interactions, such as hydrogen bonding, van der Waals forces and hydrophobic associations. The chemical or physical bondings in colloidal gels result in a stress-bearing system-spanning network topology, which leads to a solid-like mechanical response behavior. Colloidal gels, along with other colloidal systems that exhibit network structures, hold significant utility in a variety of industrial applications, ranging from food production,[25] construction industry[26] and cosmetics manufacturing[27] to targeted drug delivery.[28] Further exploration into the physical principles governing colloidal networks can offer new insights for designing colloidal materials and expand their range of applica-

[†]Corresponding author. E-mail: liufuzhou16@mails.ucas.edu.cn

[‡]Corresponding author. E-mail: fye@iphy.ac.cn

[§]Corresponding author. E-mail: mcyang@iphy.ac.cn

tions.

In this paper, we employ a simplified rough disk model to explore the effects of time-reversal symmetry-breaking interparticle friction on the structural and mechanical properties of colloids. Through Brownian dynamics simulations, we manipulate various system parameters to dissect the influence of frictional hysteresis within colloidal systems. The outcomes and subsequent analyses are systematically presented in Section 3. We find that the breaking of instantaneous time-reversal symmetry by tangential frictional interactions induces the formation of a large-scale colloidal network structure. Furthermore, these novel network structures exhibit unique physical properties, such as repulsive depletion forces and viscoelastic properties that resemble those of linear flexible polymer solutions, which highlight their multi-scale mechanical response behavior and distinguish them from other common colloidal network materials.

Our investigation commences with an examination of the effects of interparticle frictional hysteresis on colloidal structure and phase transitions. This is followed by an evaluation of its implications for the mechanical properties of colloids, encompassing depletion forces, tracer particle diffusion, and rheological behavior, highlighting distinctions from conventional colloidal gels. In Section 4, we summarize the study's findings and propose open questions and future research directions.

2. Methods

2.1. Basic setup of simulation

We consider a two-dimensional system consisting of disk-like colloid particles with rough surfaces. The pairwise central interactions among these particles are modeled using a potential that combines short-range repulsion with long-range attraction, as proposed by Frenkel *et al.*[29] This potential is represented as follows:

$$U(r)=\begin{cases}\varepsilon\alpha\left[\left(\frac{\sigma}{r}\right)^2-1\right]\left[\left(\frac{r_c}{r}\right)^2-1\right]^2, & r\le r_c,\\ 0, & r>r_c,\end{cases} \tag{1}$$

where ε denotes the potential well depth, α is the normalization constant, σ is the diameter of the particle, and r_c signifies the cutoff distance of the potential.

In the absence of particle roughness, the motion of the particle system is governed by the following Langevin equations:[30–32]

$$\begin{aligned}&\frac{\mathrm{d}\boldsymbol{r}_i}{\mathrm{d}t}=\boldsymbol{v}_i,\ \ m\frac{\mathrm{d}\boldsymbol{v}_i}{\mathrm{d}t}=-\nabla_{\boldsymbol{r}_i}U-\zeta^{\mathrm{t}}\boldsymbol{v}_i+\sqrt{2k_{\mathrm{B}}T\zeta^{\mathrm{t}}}\boldsymbol{\eta}_i^{\mathrm{t}}(t),\\ &I\frac{\mathrm{d}\omega_i}{\mathrm{d}t}=-\zeta^{\mathrm{r}}\omega_i+\sqrt{2k_{\mathrm{B}}T\zeta^{\mathrm{r}}}\eta_i^{\mathrm{r}}(t).\end{aligned} \tag{2}$$

Here, i denotes the index of particles, the mass of the particle is denoted by m, and the position, velocity, and angular velocity of particle i are represented by $\boldsymbol{r}_i$, $\boldsymbol{v}_i$, and ω_i, respectively. The moment of inertia of the particles is given by $I=\frac{1}{8}m\sigma^2$.

The environmental friction coefficients for translation and rotation are denoted by ζ^{t} and ζ^{r}, respectively, which are related by the formula[33] $\zeta^{\mathrm{r}}=\frac{1}{3}\sigma^2\zeta^{\mathrm{t}}$. The translational random force $\boldsymbol{\eta}_i^{\mathrm{t}}$ and rotational random force η_i^{r} are Gaussian distributed white noises, satisfying

$$\begin{aligned}&\langle\eta_{i,\lambda}^{\mathrm{t}}\rangle=0,\ \ \langle\eta_i^{\mathrm{r}}\rangle=0,\ \ \langle\eta_{i,\lambda}^{\mathrm{t}}(t)\eta_{j,\mu}^{\mathrm{t}}(t')\rangle=\delta_{ij}\delta_{\lambda\mu}\delta(t-t'),\\ &\langle\eta_i\eta_j^{\mathrm{r}}(t')\rangle=\delta_{ij}\delta(t-t'),\end{aligned} \tag{3}$$

where $\lambda,\mu\in\{x,y\}$ are the Cartesian component indices.

2.2. Inter-particle tangential frictional interactions

To account for the inter-particle tangential friction effect, we incorporate the tangential interaction mechanism derived from the bounce-back collision model of rough disks.[32] This model posits that as two particles come into proximity, a tangential impulse $\delta\boldsymbol{p}_{ij}^{\perp}$ is exerted on the pair, the magnitude of which is determined by the relative tangential velocity $\boldsymbol{v}_{ij}^{\perp}$ at the point of contact, as illustrated by Fig. 1(a) and quantitatively depicted by the following equation:

$$\delta\boldsymbol{p}_{ij}^{\perp}=-m\frac{\kappa}{1+\kappa}\boldsymbol{v}_{ij}^{\perp}. \tag{4}$$

Here $\delta\boldsymbol{p}_{ij}^{\perp}$ denotes the impulse exerted on particle i by particle j, and the parameter κ is defined as $\kappa:=\frac{4I}{m\sigma^2}$. By substituting I with $\frac{1}{8}m\sigma^2$ we obtain $\kappa=0.5$. The relative tangential velocity can be calculated by

$$\boldsymbol{v}_{ij}^{\perp}=\boldsymbol{v}_{ij}-\frac{1}{r_{ij}^2}(\boldsymbol{v}_{ij}\cdot\boldsymbol{r}_{ij})\boldsymbol{r}_{ij}-\frac{1}{2}(\omega_i+\omega_j)\times\boldsymbol{r}_{ij}, \tag{5}$$

where $\boldsymbol{r}_{ij}=\boldsymbol{r}_i-\boldsymbol{r}_j$ and $\boldsymbol{v}_{ij}=\boldsymbol{v}_i-\boldsymbol{v}_j$ are the relative position and velocity vector of the particle pair, respectively. After collision, the instantaneous velocity and angular velocity of the particle are changed to

$$\begin{aligned}\boldsymbol{v}_i'&=\boldsymbol{v}_i+\frac{\delta\boldsymbol{p}_{ij}^{\perp}}{m},\\ \omega_i'&=\omega_i-\frac{1}{2I}\boldsymbol{r}_{ij}\times\delta\boldsymbol{p}_{ij}^{\perp}.\end{aligned} \tag{6}$$

By definition, the bounce-back collision happens only when two particles are approaching each other and the distance of separation r_{ij} is within a cutoff distance r_{f}. In essence, the conditions for the occurrence of a bounce-back collision event are encapsulated by the following criteria:

$$\boldsymbol{r}_{ij}\cdot\boldsymbol{v}_{ij}<0\ \text{ and }\ r_{ij}<r_{\mathrm{f}}. \tag{7}$$

In the context of colliding particles, it is important to recognize that reversing the direction of the particle velocities, $\boldsymbol{v}_i\to-\boldsymbol{v}_i$, would violate the collision criteria. Consequently, the bounce-back collision mechanism introduces a tangential interaction that breaks the instantaneous time-reversal symmetry. This time-reversal symmetry breaking is characteristic of load-dependent frictional hysteresis phenomena, where the behavior of the system is sensitive to the direction of the applied force.

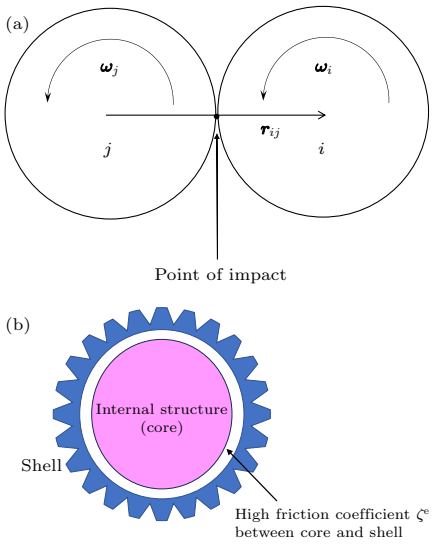

Fig. 1. (a) Illustration of bounce-back collision model. (b) Internal structure of particles in IRD system.

Considering the coupling of translational and rotational degrees of motion, as shown in Eq. (5), it is desirable to minimize this coupling to accentuate the role of tangential interactions on the translational dynamics. This can be achieved by facilitating a rapid relaxation of the rotational angular momentum in comparison to the translational momentum, which can be realized by an additional internal angular-momentum-dissipating mechanism within the particles, as illustrated in Fig. 1(b). In the limit that the rotational angular momentum rapidly dissipates to zero, the coupling between translational and rotational motion becomes negligible, hence the Langevin equation and collision dynamics for the translational motion of the system can be succinctly represented as follows:

$$\begin{aligned} &\frac{\mathrm{d}\boldsymbol{r}_i}{\mathrm{d}t} = \boldsymbol{v}_i, \quad m\frac{\mathrm{d}\boldsymbol{v}_i}{\mathrm{d}t} = -\nabla_{\boldsymbol{r}_i} U - \zeta^{\mathrm{t}}\boldsymbol{v}_i + \sqrt{2k_{\mathrm{B}}T\zeta^{\mathrm{t}}}\boldsymbol{\eta}_i^{\mathrm{t}}(t), \\ &\boldsymbol{v}_i' = \boldsymbol{v}_i - \frac{\kappa}{1+\kappa}\left(\boldsymbol{v}_{ij} - \frac{1}{r_{ij}^2}(\boldsymbol{v}_{ij}\cdot\boldsymbol{r}_{ij})\boldsymbol{r}_{ij}\right). \end{aligned} \tag{8}$$

We designate the system that evolves in accordance with Eq. (8) as an IRD system, which stands for "irreversible rough disk" system. In contrast, a system evolving according to the standard Langevin Eq. (2), in the absence of interparticle friction, is referred to as an SD system, short for "smooth disk" system. We remark that for the SD system, the translational dynamics and rotational dynamics are decoupled, hence the evolution of the translational degrees of freedom is governed by the first two equations in the Langevin Eq. (2). We perform Brownian dynamics simulations for both systems, and by comparing the outcomes of the IRD system with those of the standard SD system, we can elucidate the influence of time-reversal-symmetry-breaking friction on colloidal systems. In our implementation of the bounce-back collision model, we assess collisions between particles at each simulation time step.

From Eq. (8), it is evident that the IRD collision dynamics exhibits dissipative (frictional) characteristics, which is in stark contrast to the original bounce-back collisions that conserve kinetic energy. This distinction underscores the energy loss during collisions in the IRD system due to the frictional impulses involved.

An alternative approach to realize tangential frictional interactions is through implementation of a tangential force model, as proposed by Vitelli *et al.*[34] In this model, the tangential force exerted on particle i by particle j is mathematically expressed as

$$\boldsymbol{F}_{ij}^{\perp} = -\zeta^{\perp}\boldsymbol{v}_{ij}^{\perp}, \tag{9}$$

with $\zeta^{\perp} > 0$ a coefficient controlling the tangential interaction strength, which can be altered continuously. By substituting the bounce-back collision characteristic of the IRD dynamics with the tangential force given by Eq. (9) and retaining the interacting criteria (7), we derive an alternative model, which we refer to as the IRDF (irreversible rough disk with force) model.

In the simulation, we non-dimensionalize the particle mass and diameter by setting $m = 1$ and the particle diameter to $\sigma = 2$, and the moment of inertia is set to $I = 0.5$. The potential well depth is normalized to $\varepsilon = 1$, serving as the energy scale for the system, and $\tau = \sqrt{m(\sigma/2)^2/\varepsilon}$ fixes the time unit. The potential cutoff distance r_{c} and tangential interaction cutoff distance r_{f} are set to the same value, $r_{\mathrm{c}} = r_{\mathrm{f}} = 1.2\sigma$. The temperature range is varied from $k_{\mathrm{B}}T = 0.1$ to $k_{\mathrm{B}}T = 2.0$, and particle packing fraction ϕ varies from $\phi = 0.05$ to $\phi = 0.5$. The environmental translational and rotational friction coefficients are assigned as $\zeta^{\mathrm{t}} = 100$ and $\zeta^{\mathrm{r}} = 400/3$, respectively. For the IRDF model, unless specified otherwise, the coefficient $\zeta^{\perp}$ is assigned the value $\zeta^{\perp} = \zeta^{\mathrm{t}} = 100$.

The simulation time step, in units of τ, is defined as $\Delta t = 0.002$. The simulations are conducted in a box with edge lengths $L_x = L_y = 100$, employing periodic boundary conditions. For all simulations, the system is initialized with a random configuration and evolves $\sim 10^8$ time steps until a steady state is reached. A useful time scale in Brownian simulations is the Brownian relaxation time τ_{R}, defined as

$$\tau_{\mathrm{R}} = \frac{\sigma^2}{4D}, \tag{10}$$

where D is the diffusion constant of a free Brownian particle. By substituting the Stokes–Einstein relation $D\zeta^{\mathrm{t}} = k_{\mathrm{B}}T$ into Eq. (10), we obtain $\tau_{\mathrm{R}} = 100/(k_{\mathrm{B}}T) = 5\times 10^4 \Delta t/(k_{\mathrm{B}}T)$.

2.3. Measurement of effective interaction between test particles

To measure the depletion force generated by the colloid system, we put two large test particles with diameter $\sigma' = 5\sigma$ into the system and keep their positions $\boldsymbol{R}_1$, $\boldsymbol{R}_2$ at a fixed distance d. The colloid particles interact with the test particles

through 12-24 WCA potential,[35] which is expressed as

$$U_{\mathrm{WCA}}(r)=\begin{cases}4\varepsilon\left[\left(\frac{\tilde{\sigma}}{r}\right)^{24}-\left(\frac{\tilde{\sigma}}{r}\right)^{12}\right]+\varepsilon & r<2^{1/12}\tilde{\sigma},\\ 0, & r\geq 2^{1/12}\tilde{\sigma},\end{cases} \tag{11}$$

where $\tilde{\sigma}=(\sigma+5\sigma)/2=3\sigma$ is the distance at contact between the center of a colloid particle and a test particle. The depletion force acting on test particle 1 (and similarly for test particle 2) is calculated as the mean force exerted by all colloid particles on that specific test particle. These forces are denoted as $\boldsymbol{F}_1$ for test particle 1 and $\boldsymbol{F}_2$ for test particle 2. Typically $\boldsymbol{F}_1$ and $\boldsymbol{F}_2$ are equal in magnitude but opposite in direction, and we can denote the depletion force by the magnitude of either force, projected along the line connecting the two test particles, namely,

$$F_{\mathrm{dep}}=\boldsymbol{F}_1\cdot\frac{\boldsymbol{R}_{12}}{|\boldsymbol{R}_{12}|}=\boldsymbol{F}_2\cdot\frac{\boldsymbol{R}_{21}}{|\boldsymbol{R}_{21}|}, \tag{12}$$

where $\boldsymbol{R}_{12}=\boldsymbol{R}_1-\boldsymbol{R}_2$ is the vector pointing from particle 2 to particle 1, and $\boldsymbol{R}_{21}$ is defined similarly. It is evident from the definition that a positive depletion force $F_{\mathrm{dep}}>0$ indicates a repulsive interaction between the test particles, while $F_{\mathrm{dep}}<0$ suggests an attractive interaction. This distinction is essential for characterizing the nature of the forces within the colloidal system.

2.4. Measurement of tracer diffusion

In order to investigate the diffusion property of the colloid system, we insert a large tracer Brownian particle into the system, and allow the tracer particle to interact with surrounding colloidal particles via the WCA potential $U_{\mathrm{WCA}}(r)$. Once the colloid system has reached a steady state, we measure the mean squared displacement (MSD) $\langle\Delta r^2\rangle$ of the tracer to reveal the impact of the surrounding colloids on the tracer particle's diffusion behavior.

The MSD of a Brownian particle diffusing in a two-dimensional system typically follows a power-law relationship with time

$$\langle\Delta r^2(t)\rangle=4D_\beta t^\beta, \tag{13}$$

where D_β represents the generalized diffusion coefficient, and β is the exponent of anomalous diffusion.

In the MSD measurement, the diameter of the tracer particle is set to match that of the test particle used in the depletion force measurement, $\sigma'=5\sigma$. The friction experienced by the tracer particle is determined by the translational friction coefficient $\zeta_{\mathrm{tr}}^{\mathrm{t}}=5\zeta^{\mathrm{t}}=500$, resulting in $\zeta_{\mathrm{tr}}^{\mathrm{r}}=2000/3$.

2.5. Rheological measurements

To perform rheological measurements, we utilize the Lees–Edwards boundary condition,[32,36–38] which allows us to apply periodic shear to the colloidal system, thereby facilitating the study of its viscoelastic properties. Assuming a sinusoidal shear strain $\gamma(t)=\gamma_0\sin(\omega t)$ being exerted on the system, the mechanical response of the viscoelastic system can be captured by the following equation:

$$\sigma(t)=\gamma_0[G'(\omega)\sin(\omega t)+G''(\omega)\cos(\omega t)], \tag{14}$$

where ω and γ_0 represent the angular frequency and magnitude of the shear, respectively, $\sigma(t)$ is the magnitude of the shear stress and G' and G'' denote the storage (elasticity) modulus and loss (viscosity) modulus of the system, respectively. Accordingly, after subjecting the system to n cycles of shear, the viscoelastic modulus of the system can be calculated by the following formula:[39–41]

$$\begin{aligned}G'(\omega)&=\frac{\omega}{n\pi\gamma_0}\int_0^{\frac{2n\pi}{\omega}}\sigma(t)\sin(\omega t)\,\mathrm{d}t,\\ G''(\omega)&=\frac{\omega}{n\pi\gamma_0}\int_0^{\frac{2n\pi}{\omega}}\sigma(t)\cos(\omega t)\,\mathrm{d}t.\end{aligned} \tag{15}$$

In the rheological measurement, we apply shear to the system along x direction, and the shear stress σ_{xy} is measured using Irving–Kirkwood formula[42,43]

$$\sigma_{\lambda\mu}=-\frac{1}{A}\sum_i m\tilde{v}_{i,\lambda}\tilde{v}_{i,\mu}-\frac{1}{2A}\sum_{i\neq j}r_{ij,\lambda}F_{ij,\mu}. \tag{16}$$

Here, $A=L_x\cdot L_y$ is the area of the simulation box, and $\tilde{v}_{i,\lambda}$, $r_{ij,\lambda}$ and $F_{ij,\lambda}$ represent the Cartesian component of particle peculiar velocity $\tilde{\boldsymbol{v}}_i$, pairwise relative position $\boldsymbol{r}_{ij}$ and pairwise force $\boldsymbol{F}_{ij}$ (exerted on particle i by particle j), respectively, with the Cartesian indices $\lambda,\mu\in\{x,y\}$. The particle peculiar velocity is the difference between the particle velocity $\boldsymbol{v}$ and the mean flow velocity $\boldsymbol{u}$ at the particle position $\boldsymbol{r}_i$, and is calculated by

$$\tilde{\boldsymbol{v}}_i=\boldsymbol{v}_i-\boldsymbol{u}(\boldsymbol{r}_i,t). \tag{17}$$

The inter-particle force $\boldsymbol{F}_{ij}$ is a combination of contribution of the potential force and the tangential frictional interaction between particles, namely,

$$\boldsymbol{F}_{ij}=\boldsymbol{F}_{ij}^{\mathrm{pot}}+\boldsymbol{F}_{ij}^{\perp}=-\nabla_{\boldsymbol{r}_i}U(r_{ij})+\boldsymbol{F}_{ij}^{\perp}. \tag{18}$$

When the tangential interaction is modeled by the bounce-back collision mechanism (i.e., IRD systems), the (effective) tangential frictional force in Eq. (18) can be quantified in terms of collisional impulses $\delta\boldsymbol{p}_{ij}^{\perp}$ [Eq. (4)] and simulation time step Δt as

$$\boldsymbol{F}_{ij,\mathrm{eff}}^{\perp}=\frac{\delta\boldsymbol{p}_{ij}^{\perp}}{\Delta t}. \tag{19}$$

In other scenarios where the frictional force model is employed (i.e., in IRDF systems), we can use formula (9) to incorporate the tangential frictional forces directly.

During the rheological measurements, for each simulation frame, we collect the instantaneous velocities $\boldsymbol{v}_i(t)$ and positions $\boldsymbol{r}_i(t)$ of the colloidal particles, along with the forces $\boldsymbol{F}_{ij}(t)$ acting on them. We then perform the summation described in Eq. (16), with the summation indices i, j spanning across all particle indices, obtaining the instantaneous stress tensor $\sigma_{\lambda\mu}(t)$. Subsequently, we apply a Fourier transform [Eq. (15)] to extract the storage modulus G' and the loss modulus G''. In the measurement, the shear strain magnitude γ_0 is set to $\gamma_0 = 1\%$, and the shear cycle number n is set to $n = 500$.

3. Results and discussion

3.1. Structure behavior

The phase diagram and steady state configurations of the IRD system are exhibited in Fig. 2. The IRD system displays a remarkable linear chain-like order in low density regime ($\phi \lesssim 0.3$), as shown in Fig. 2(b). At moderate densities ($\phi \simeq 0.3$), a large-scale, system-spanning network structure emerges in the system, which is formed by the crosslinking of extended colloidal chains [see Fig. 2(c)]. As the density increases further, the network structure undergoes a coarsening process, transforming into a foam-like configuration, as shown in Fig. 2(d). To classify the structural phases, we distinguish between fluid and chain/network states based on the presence of colloidal chains consisting of more than four particles. In fluid states, these chains are rare or absent, while in chain/network states, they are a predominant feature. The foam state is characterized by extensively connected colloidal networks, which evolve from coarsened colloidal chains. The key difference between the foam state and the chain/network state is the integration of particles into the network: in the foam state, nearly all particles are part of the system-spanning network, whereas in the chain/network state, a significant fraction of particles remains unincorporated and isolated.

In contrast, the SD system exhibits typical equilibrium phase behavior: the phase diagram of the SD system consists of fluid phase and hexagonal crystalline solid phase, as illustrated by Fig. 3. As the temperature rises, the solid state transitions into a fluid state, illustrating the classic behavior of melting, with no linear order or network structure present in the system. A noteworthy observation is that, at low temperatures and intermediate densities, the SD system exhibits a "solid-like network" state, as shown in Fig. 3(b). This state is characterized by the coexistence of two distinct features: local hexagonal arrangement of particles inside the coarse chains and a global-scale network structure. This phase is indicative of metastable states in particle systems with strong attractive forces at low temperatures, where the system settles into a local potential energy minimum, displaying localized crystalline order. The low temperature hinders the system's ability to achieve a global energy minimum within a reasonable time scale, leading to the formation of this hybrid structural phase.

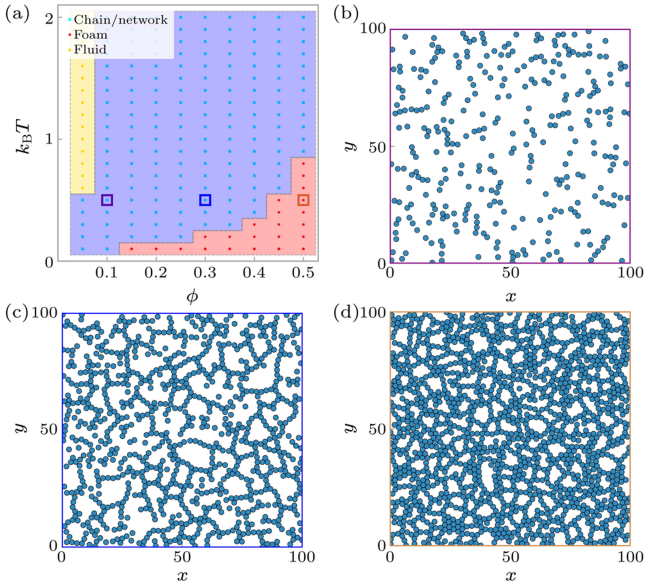

Fig. 2. Phase behavior of the IRD system. (a) Phase diagram of the IRD system, in which the horizontal axis represents the packing fraction ϕ and the vertical axis represents the temperature k_BT. The red-shaded, purple-shaded and yellow-shaded areas stand for the foam state, the chain/network state and the pure fluid state, respectively. (b)–(d) Typical snapshots of the IRD system at temperature $k_BT = 0.5$ and packing fraction $\phi = 0.1$ (b), 0.3 (c), 0.5 (d).

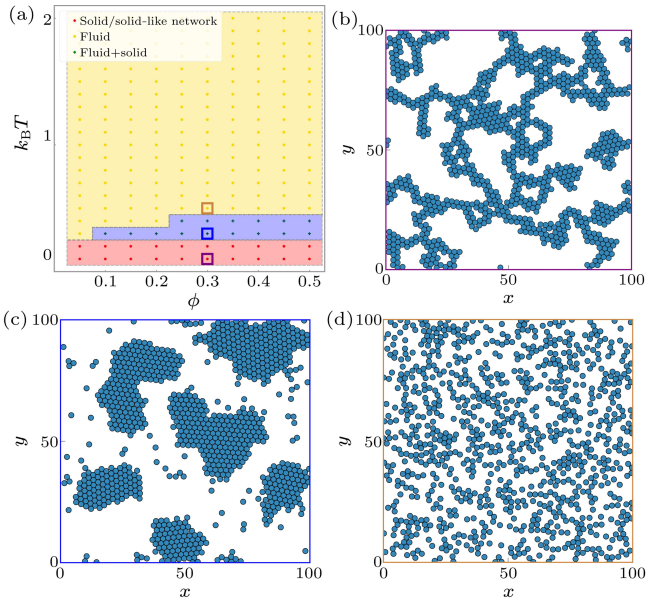

Fig. 3. Phase behavior of the SD system. (a) Phase diagram of the SD system, in which the horizontal axis represents the packing fraction ϕ and the vertical axis represents the temperature k_BT. The red-shaded area represents the solid and the solid-like network states, while the purple-shaded and yellow-shaded areas stand for the solid–fluid coexistence state and the pure fluid state, respectively. (b)–(d) Typical snapshots of the SD system at packing fraction $\phi = 0.3$ and temperature $k_BT = 0.1$ (b), 0.3 (c), 0.5 (d).

We further quantify the linear order in the IRD system by computing the radial distribution function (RDF)[44] $g(r)$ and the bond orientational order parameter ψ_k (for $k = 2$ and 6). The bond orientation order parameter ψ_k of particle i in the system is determined using the formula[45–47]

$\psi_k(i) = (1/N_i)\sum_j \exp(\mathrm{i}k\theta_{ij})$, in which j runs over all neighboring particles of particle i, and θ_{ij} denotes the angle between the separation vector $\boldsymbol{r}_{ij}$ and the x-axis. To calculate the ψ_k, the python package freud[48] is utilized.

Figure 4 presents the radial distribution function and the distribution of bond orientational order parameter in a typical network configuration at temperature $k_\mathrm{B}T = 0.5$ and packing fraction $\phi = 0.3$. It is clear from Fig. 4(b) that the positions r_ℓ of the first five peaks in radial distribution function $g(r)$ manifest a linear arrangement, such that $r_\ell = \ell \cdot r_1$ for $1 \le \ell \le 5$. This pattern underscores the significant linear order inherent in the spatial arrangement of the colloidal network structure, indicating its quasi-one-dimensional (1D) character. The quasi-one-dimensional character of the network structure is also evident from the plots of the bond orientational order parameter [Figs. 4(c) and 4(d)], which suggests an absence of hexagonal order (characterized by ψ_6) and the presence of strong linear order (characterized by ψ_2).

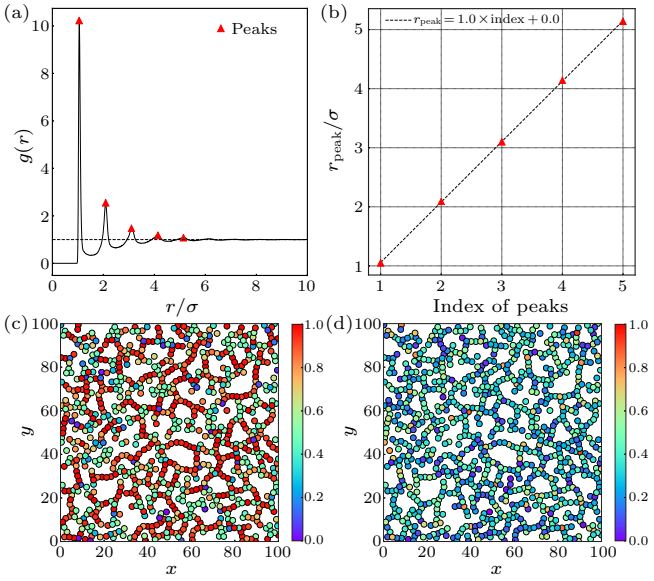

Fig. 4. Typical radial distribution function and local bond orientation order parameter of the IRD system in network phase. (a) Radial distribution function $g(r)$. The red triangles indicate the peaks of $g(r)$. (b) Peak position r_{peak} of the radial distribution function as a function of peak index. Black dashed line indicates the linear fit of r_{peak} versus peak index. (c)–(d) Local bond orientation order parameter ψ_k (absolute value): (c) $|\psi_2|$, (d) $|\psi_6|$.

The alternative IRDF model of tangential interactions displays similar structural characteristics to the IRD system, as illustrated by Fig. 5. A key difference, however, is observed in the phase diagram of Fig. 5(a), where the region dominated by linear order and network structure is relatively reduced in comparison to that of the IRD system. Furthermore, at high densities and low temperatures, the IRDF model accommodates coexisting states of a hexagonal crystalline phase with colloidal chain-like structures, as shown in Fig. 5(d). These distinctions suggest that the effect of tangential forces on the system's structure is less pronounced than the impact of collisional impulses. This can be explained by the abrupt and instantaneous character of the collisional model, which exerts a more dramatic and immediate alteration to the system's dynamics.

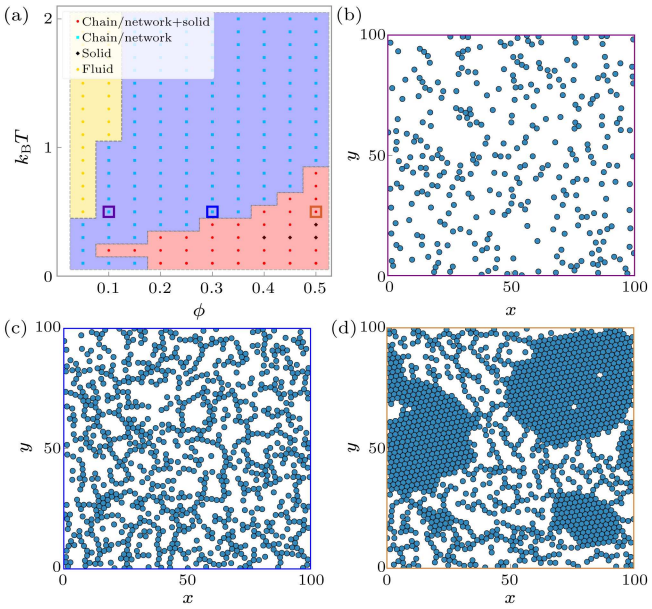

Fig. 5. Phase behavior of the IRDF system. (a) Phase diagram of the IRDF system, in which the horizontal axis represents the packing fraction ϕ and the vertical axis represents the temperature $k_\mathrm{B}T$. The red-shaded area represents the solid state and the coexistence state of chain/network structure and solid phase, while the purple-shaded and yellow-shaded areas stand for the chain/network state and the pure fluid state, respectively. (b)–(d) Typical snapshots of IRDF system at temperature $k_\mathrm{B}T = 0.5$ and packing fraction $\phi = 0.1$ (b), 0.3 (c), 0.5 (d).

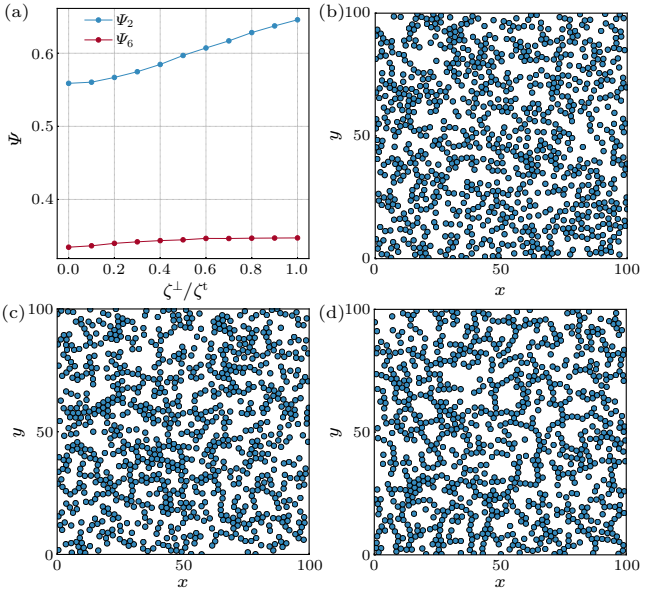

Fig. 6. Relation between structure of the IRDF system and tangential interaction strength at temperature $k_\mathrm{B}T = 0.5$ and packing fraction $\phi = 0.3$. (a) Global average of bond orientational order parameters Ψ_2 and Ψ_6 at different $\zeta^\perp/\zeta^\mathrm{t}$. (b)–(d) Typical snapshots of the IRDF system with $\zeta^\perp/\zeta^\mathrm{t} = 0.1$ (b), 0.5 (c), 1.0 (d).

Given that the translational and rotational degrees of freedom are uncoupled in both SD and IRD systems, it follows that the primary distinction between these two systems lies in the tangential interactions between particles. To investigate the impact of tangential interactions on the structure change

of the colloid system, we may make use of the alternative IRDF model, in which the tangential interaction strength can be easily adjusted. The simulation results of steady-state system structure with different $\zeta^{\perp}$ values of the IRDF system at moderate temperature $k_{\mathrm{B}}T = 0.5$ and packing fraction $\phi = 0.3$ are shown in Fig. 6. One can observe that the linear order arises in the initially homogeneous fluid system with the increase of $\zeta^{\perp}$ value, culminating in the formation of a large-scale network structure, a distinctive trait of both the IRD and IRDF systems. These results reveal the key role that tangential interactions play in the formation of network structures.

Now we have demonstrated the fundamental effect of tangential interaction on the formation of network structures. Keeping in mind that the tangential frictional interaction in the IRD system breaks the instantaneous time-reversal symmetry, a compelling question arises: to what extent does this symmetry-breaking effect influence the structural transitions within the colloidal system?

To address this question, we perform a series of auxiliary simulations of IRD systems with modifications. In these simulations, the collision criteria are adjusted to account for the possibility of collision events during separation when particles are within the collision cutoff distance r_{f}. Specifically, during approach (where $\boldsymbol{r}_{ij} \cdot \boldsymbol{v}_{ij} < 0$ and $r_{ij} < r_{\mathrm{f}}$), a collision is guaranteed to occur. Conversely, during separation (where $\boldsymbol{r}_{ij} \cdot \boldsymbol{v}_{ij} > 0$ and $r_{ij} < r_{\mathrm{f}}$), a bounce-back collision takes place with a probability p. The dimensionless parameter $0 \leq p \leq 1$ controls the degree of time-reversal-symmetry-breaking in the tangential interactions. The case $p = 1$ corresponds to a perfect time-reversal symmetry in tangential interactions, and as p approaches 0 (i.e., as $1 - p$ approaches 1), the system experiences an increasing extent of time-reversal-symmetry-breaking. The results of the auxiliary simulations are shown in Fig. 7, in which the temperature and packing fraction are set to $k_{\mathrm{B}}T = 0.5$ and $\phi = 0.3$. Figures 7(a) and 7(b) illustrate that when the tangential interaction mechanism is reversible, i.e., $p \simeq 1$, the steady state of the system assumes a hexagonal crystalline solid phase. A comparison with Fig. 6(b) reveals that instantaneous-time-reversal-symmetric tangential interactions enhance the isotropic attraction among colloid particles. However, as the quantity $1 - p$ exceeds 0.3, i.e., when time-reversal-symmetry-breaking increases beyond a threshold, a linear order spontaneously emerges in the initial hexagonal crystalline solid state system [Fig. 7(c)]. This transition eventually leads to the formation of a system-spanning network structure [Fig. 7(d)], which is a characteristic feature of the IRD system. These findings suggest that the time-reversal-breaking in tangential frictional interactions is pivotal in the emergence of linear order and instigates the self-assembly processes of network structures within IRD systems.

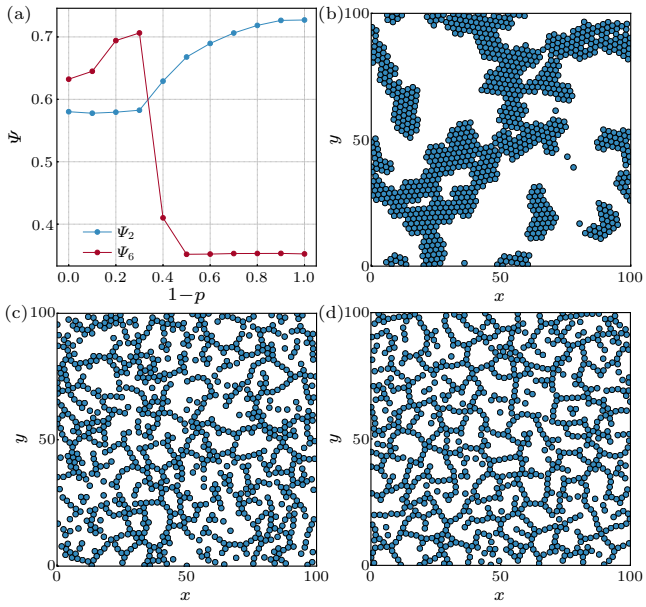

Fig. 7. Relation between structure of the IRD system and p value at temperature $k_{\mathrm{B}}T = 0.5$ and packing fraction $\phi = 0.3$. (a) Global average of bond orientational order parameters Ψ_2 and Ψ_6 at different p values. (b)–(d) Typical snapshots of IRD system with $1 - p = 0.1$ (b), 0.5 (c), 0.9 (d).

We next examine the kinetics of network structure forming processes, which is characterized by the temporal evolution of aggregation number N_{agg} and global average Ψ_k of the bond orientational order parameter of the system, starting from a random initial configuration. Two particles are considered part of the same aggregation if their distance is within

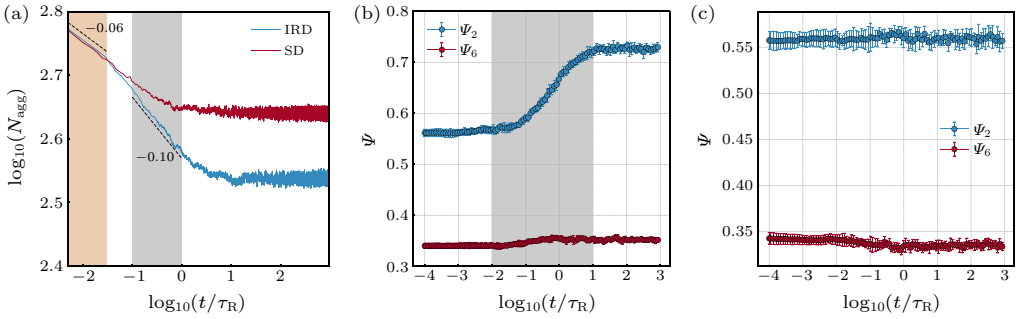

Fig. 8. Temporal evolution of the structure of colloidal systems at temperature $k_{\mathrm{B}}T = 0.5$ and packing fraction $\phi = 0.3$. (a) Evolution of aggregation number in the system. The yellow and gray shaded areas indicate the typical exponential decay regimes of early and intermediate stages of evolution, respectively, and the black dashed line indicates the power law fit in each regime. (b) and (c) Temporal evolution of global bond-orientational order parameters Ψ_2 and Ψ_6. (b) The IRD system. The gray shaded area indicates the characteristic evolution time period of the system. (c) The SD system.

the cutoff distance $r_c = r_f = 1.2\sigma$. As exhibited in Fig. 8, the aggregation kinetics and bond orientation order kinetics both display evident differences between the IRD and SD systems. For aggregation kinetics [Fig. 8(a)], both IRD and SD systems exhibit a power-law relationship $N_{agg} \propto t^{-0.06}$ during the early stages of temporal evolution. However, as time progresses, the aggregation process within the IRD system accelerates, displaying a steeper power-law $N_{agg} \propto t^{-1.0}$. This discrepancy suggests that in the intermediate evolution regime, significant structural transformations take place in the IRD system, which enhances the efficiency of aggregation growth. The plots of bond orientational order parameter, Figs. 8(b) and 8(c), further confirm this speculation, which reveal a significant increase of linear order in the IRD system, while the order parameters Ψ_2 and Ψ_6 show little variation during the temporal evolution of the SD system. Another noteworthy observation is that, even in the steady state, the IRD system retains hundreds of distinct aggregations. This suggests that the system-spanning network structure does not absorb all colloidal particles, which contrasts with colloidal gels with irreversible bondings, in which every colloid particle is integrated into the network structure.[24,39]

3.2. Effective interaction between large test particles

The results of depletion force measurements are presented in Fig. 9. The depletion force generated by the IRD system in the network phase exhibits a short-range repulsive and long-range attractive character, while for the fluid state SD system, the depletion interaction is dominated by attraction, and the magnitude of depletion force is also significantly weaker than that of the IRD system. While the attractive depletion force present in the SD system can be ascribed to entropic effect,[49–52] the short-ranged repulsive depletion interactions observed in the IRD system are atypical in colloidal systems, which warrant an in-depth investigation to unravel its underlying mechanisms.

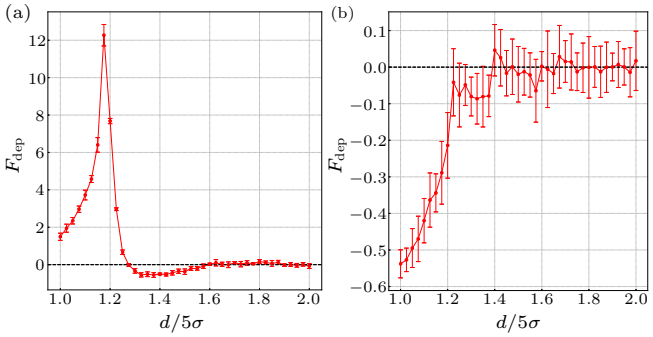

Fig. 9. Depletion force results measured at temperature $k_BT = 0.5$ and packing fraction $\phi = 0.4$. A positive value of F_{dep} indicates repulsion, while a negative value signifies attraction. (a) Depletion force generated by the IRD system in the network phase. (b) Depletion force generated by the SD system in the fluid phase.

To uncover the cause of the aforementioned short-ranged repulsive depletion interactions, we examine the colloid particle distribution in the IRD system, as illustrated in Fig. 10, which yields valuable insights into the interactions between the test particles and surrounding colloids. Figures 10(a) and 10(c) correspond to the case that the separation between test particles is $d = 5.875\sigma$, a condition at which the repulsive depletion force is maximized. On the other hand, Figs. 10(b) and 10(d) depict another scenario of particular interest, where the separation distance between the test particles is increased to $d = 7.0\sigma$, corresponding to the maximum of attractive depletion force. In the repulsive scenario, the density plot in Fig. 10(a) indicates a pronounced localization of colloidal particle density, manifesting as two distinct and intense peaks situated laterally adjacent to the contact region of the two test particles. This phenomenon can be attributed to the rigidity of the colloidal chains [Fig. 10(c)], which impedes the movement of the colloidal particles in the vicinity of the test particles' contact region, leading to the emergence of localized density peaks. Because of their locations, the density peaks exert substantial forces on the test particles in the direction that push them away, which results in a repulsive depletion interaction.

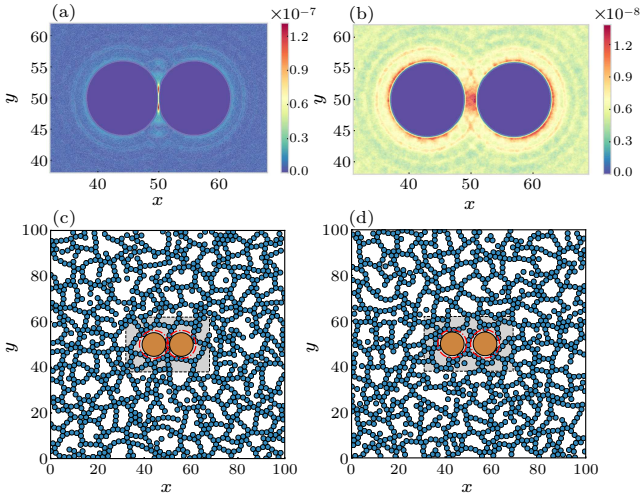

Fig. 10. Colloidal particle density distribution and particle configuration of the IRD system at temperature $k_BT = 0.5$, and packing fraction $\phi = 0.4$. (a) and (b) Spatial probability density of colloid particles around the tracers at various separations d: (a) $d = 5.875\sigma$ and (b) $d = 7.0\sigma$. (c) and (d) Typical snapshots of the IRD system. The gray shaded area indicates the spatial range of (a) and (b). The yellow shaded areas represent the size of the test particle while the red dashdot lines indicate the effective range from which small colloid particles are excluded by the presence of larger particles. (c) $d = 5.875\sigma$. (d) $d = 7.0\sigma$.

On the other hand, the lateral density peaks adjacent to the test particles' contact region vanish when the test particle separation is increased to $d = 7.0\sigma$, as shown in Fig. 10(b). In this scenario, the increased separation distance d allows the colloid chain amidst the two test particles to swing more freely, thereby reducing its contribution to the net depletion force. The net force acting on the test particles is dominated by the collective influence of two ring-like density peaks that encircle the test particles, and these ring-like density peaks are not closed, with gaps at the near ends of the test particle pair.

These gaps are a result of the rigidity of the colloidal chain between the two test particles, which acts as a barrier preventing colloid particles from entering the gap regions. As a consequence, the net force produced by the ring-like structures is attractive, and the nature of this attraction fundamentally differs from the conventional entropic forces (Asakura–Oosawa–Vrij force).[49–52]

The above measurements of the depletion force have been conducted with test particles of a fixed size. We predict that changing the size of these test particles would not qualitatively alter the general form of the depletion force and the observed trends in the above results. In the IRD system, the depletion force is a result of the interactions between the colloidal chains and the test particles. As long as the test particles' size is comparable to the persistence length of the colloidal chains, the fundamental physical scenario is preserved. While the magnitude of the depletion force may be quantitatively modified by resizing the test particles, the overall shape of the force curve is expected to remain consistent. Similarly, in the SD system, the depletion force is primarily an entropic effect, and thus, resizing the test particles does not significantly alter the shape of the force curve.

3.3. Diffusion of a large tracer

The diffusion kinetics of the tracer particle in colloidal background is presented in Fig. 11. The mean square displacement (MSD) of the tracer presents similar profiles in both IRD and SD systems, characterized by a ballistic transport $\langle \Delta r^2 \rangle \propto t^2$ in the early times and normal diffusion

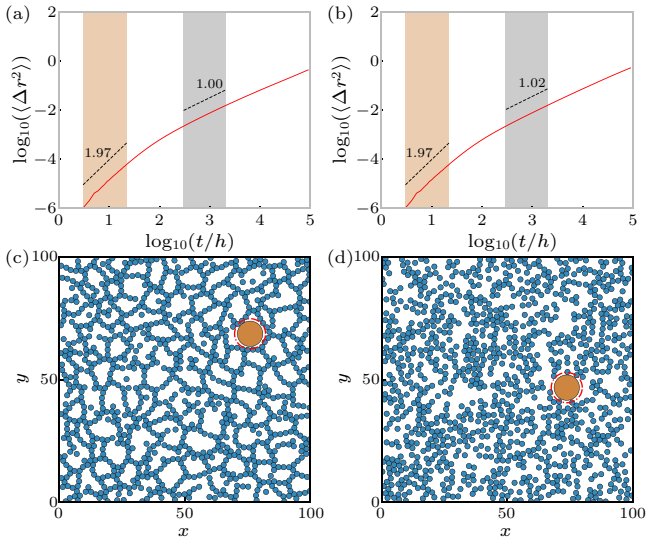

Fig. 11. (a) and (b) Mean square displacement of tracer particle in colloid background at temperature $k_BT = 0.5$ and packing fraction $\phi = 0.4$. $h = 0.002$ is the simulation time step. The yellow and gray shaded areas indicate the typical regimes of ballistic transport and normal diffusion, respectively. The black dashed lines indicate the power-law fit in typical regimes. (a) IRD system. (b) SD system. (c) and (d) Typical snapshots of tracer diffusions. The yellow shaded areas represent the nominal size of the big particle while the red dashdot lines indicate the effective range from which small colloid particles are excluded by the presence of the larger particles. (c) IRD system. (d) SD system.

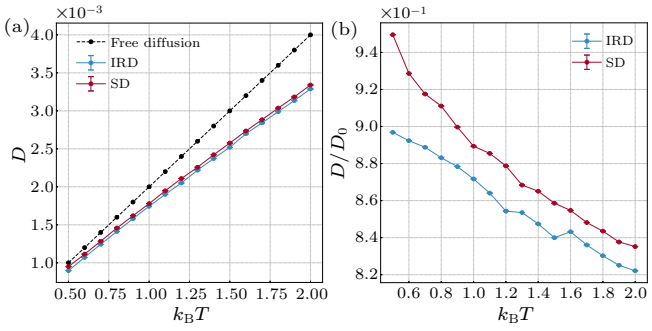

Fig. 12. Diffusion coefficient and effective friction coefficient of tracer particle at various temperatures and colloidal packing fraction $\phi = 0.4$. (a) Diffusion coefficient D of the tracer. (b) Diffusion coefficient D in units of free diffusion coefficient D_0.

$\langle \Delta r^2 \rangle = 4Dt$ in steady states. Upon examination of the typical snapshots of the IRD system in Fig. 11(c), one can observe that the tracer particle in the IRD system is trapped in a "cage" formed by colloidal chains. In contrast, as shown in Fig. 11(d), the background colloidal particles in the SD system exhibit fluid-like behavior, suggesting a higher likelihood of free diffusion of the tracer particle within this system. However, as illustrated in Fig. 12, the measured diffusion coefficients for the IRD and SD systems exhibit only minor differences. This observation implies that the "colloidal cage" structures in the IRD system are not sufficiently restrictive to exert a substantial influence on the diffusion dynamics of the tracer particle.

3.4. Rheology results

The results of rheological measurements for IRD and SD systems are shown in Fig. 13. The tested shear frequency range is $10^{-1} \leq \omega\tau_R \leq 7 \times 10^2$, and the applied shear amplitude is $\gamma_0 = 1\%$. The curve representing the loss modulus G'' is smoother than that of the storage modulus G', and the two curves run roughly parallel to each other. The loss modulus $G''(\omega)$ of the SD system exhibits a quasi-linear power law $G'' \simeq \omega^{0.97}$, indicating a Newtonian-fluid-like behavior. However, the SD system also exhibits a weak elastic response, as evidenced by $G'(\omega) \neq 0$. This behavior is similar to that of concentrated Brownian suspensions, as was reported in Refs. [53–55]. In contrast, the loss modulus of the IRD system displays a much flatter power law $G'' \simeq \omega^{0.68}$ in the low frequency regime, which suggests a non-Newtonian behavior. The magnitude of the storage modulus of the IRD system is larger than that of the SD system, which implies that the network structure of the IRD system, behaving like a loose skeleton, enhances the elasticity of the system. Moreover, examination of typical snapshots in Figs. 13(c) and 13(d) reveals that the colloidal chains within the IRD system align in accordance with the direction of shear strain. In contrast, the SD system maintains an isotropic state. This observation suggests that the IRD system is more sensitive to external perturbations than the SD system.

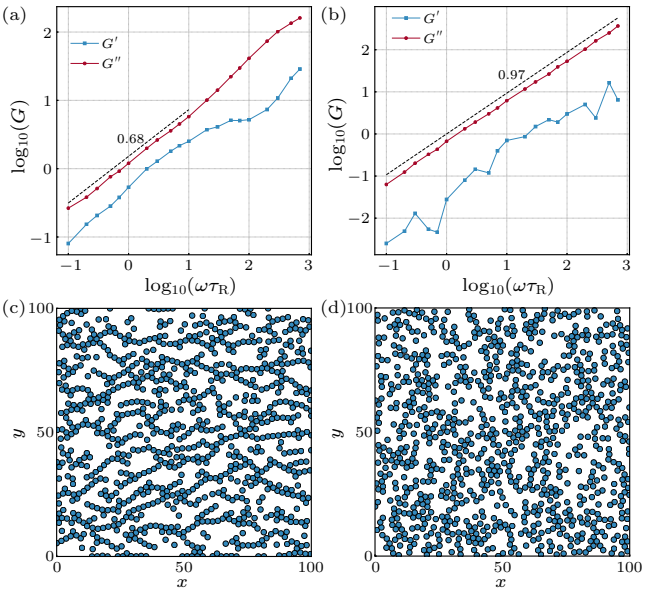

Fig. 13. Viscoelasticity modulus and typical snapshots of colloid system at temperature $k_BT = 0.5$ and packing fraction $\phi = 0.3$. The unit of shear frequency is taken as $1/\tau_R$. The black dashed lines indicate the linear fits of the viscosity modulus in the log–log plots. Viscoelasticity modulus: (a) IRD system, (b) SD system. Typical snapshots at shear frequency $\omega\tau_R = 700$: (c) IRD system, (d) SD system.

A distinctive feature of the IRD system is that the loss modulus G'' is always higher than the storage modulus G', which markedly contrasts with typical colloidal gels, where the elastic response dominates the system across the entire spectrum of shear frequencies.[56,57] This observation, together with the power law $G''(\omega) \propto \omega^{0.68}$ in the low frequency regime, suggests that the rheological properties of the IRD system resemble those of dilute solutions of linear flexible polymers, as previously reported in Refs. [58–61]. Consequently, the IRD system can be classified as a novel type of flexible colloidal networks, which is consistent with the picture that the IRD networks are susceptible to large-scale shear perturbations [Fig. 13(c)]. On the other hand, when subject to small local perturbations, the IRD system exhibits considerable rigidity, as exhibited by the depletion force measurement results in Subsection 3.2. This implies that the IRD system possesses a multi-scale mechanical response, exhibiting a combination of flexibility and rigidity that varies with the scale of applied forces.

4. Conclusions

In this paper, we delve into the intricacies of a two-dimensional nonequilibrium colloidal system, characterized by interparticle frictional interactions that break time-reversal symmetry (friction hysteresis). Our results reveal that such friction can induce the emergence of linear order and trigger the self-assembly of the colloidal system into large-scale network structures. This self-assembly process depends crucially on the disruption of time-reversal symmetry, indicating its essence as a nonequilibrium phase transition.

Furthermore, the system under investigation demonstrates a suite of unique physical properties that set it apart from traditional equilibrium colloidal systems. Notably, it manifests short-ranged repulsive depletion forces and exhibits rheological properties that are close to linear flexible polymer solutions, which reveals its multi-scale mechanical response character. These findings expand our understanding of colloidal self-assembly, highlight the fundamental role of symmetry-breaking in regulating material behavior and provide a new perspective on the design of colloidal materials with specific functionalities.

Several questions remain open for the studied systems. A primary question that needs elucidation is how time-reversal-symmetry-breaking at the microscopic level initiates and directs the bottom-up self-organization process, culminating in the formation of colloidal chains and network structures. The diffusion dynamics of the tracer particles is only weakly influenced by the tangential friction interactions, suggesting that models of rough disks presented in this paper require further modifications to probe the non-equilibrium diffusion dynamics of the colloidal systems.[62–64] Additionally, a significant challenge that warrants resolution is developing a theoretical model to describe the rheological behavior of the IRD system, which is crucial to understanding the network structure's role in the system's mechanical response.

Acknowledgements

We acknowledge the support of the National Natural Science Foundation of China (Grant Nos. 12274448, 12325405, and 12174390) and the National Key R&D Program of China (Grant No. 2022YFF0503504). Data analysis of the bond order parameters for this publication utilizes the freud library.[48]

References

[1] Rahman M A and Beltramo P 2023 *Front. Phys.* **11** 1248706
[2] Hu M, Hsu C P and Isa L 2020 *Langmuir* **36** 11171
[3] Li Z, Cao M, Li P, Zhao Y, Haoyu B, Wu Y and Jiang L 2019 *Matter* **1** 661
[4] Wang H, Nobes D and Vehring R 2019 *Pharm. Res.* **36** 43
[5] Chen W, Yu B, Zhang X, Zhang F, Zan X and Li T 2022 *Journal of Colloid and Interface Science* **629** 173
[6] Derjaguin B V, Muller V M and Toporov Y P 1975 *Journal of Colloid and Interface Science* **53** 314
[7] Violano G, Demelio G and Afferrante L 2018 *Procedia Structural Integrity* **12** 58
[8] Popov V, Li Q, Lyashenko I and Pohrt R 2021 *Friction* **9** 1688
[9] Deng Z, Smolyanitsky A, Li Q, Feng X Q and Cannara R 2012 *Nat. Mater.* **11** 1032
[10] Egberts P, Han G, Liu X, Johnson A T C and Carpick R 2014 *ACS Nano* **8** 5010
[11] Ye Z, Egberts P, Han G, Johnson A T C, Carpick R and Martini A 2016 *ACS Nano* **10** 5161
[12] Gong P, Ye Z, Yuan L and Egberts P 2018 *Carbon* **132** 749
[13] Wang Y, Ding J, Fan Z, Tian L, Li M, Lu H, Zhang Y, En M, Li J and Shan Z 2021 *Nat. Mater.* **20** 1
[14] Sattari B, Pitkar A, Ye Z and Nalam P 2022 *Advanced Materials Interfaces* **9** 2201249
[15] Xu C, Ye Z and Egberts P 2023 *npj 2D Materials and Applications* **7** 1
[16] Xu C, Ye Z and Egberts P 2023 *Applied Surface Science* **630** 157442

[17] Souza A and Tao M 2018 *European Journal of Applied Mathematics* **30** 830
[18] Meester V and Kraft D 2016 *Langmuir* **32** 10668
[19] Allard J, Burgers S, Rodríguez González M, Zhu Y, Feyter S and Koos E 2022 *Colloids and Surfaces A: Physicochemical and Engineering Aspects* **648** 129224
[20] Kato A, Jiang Y, Chen W, Seto R and Li T 2023 *Journal of Colloid and Interface Science* **641** 492
[21] Spatafora A, Lobmeyer D, Hildebrand Pires da Cunha L, Joshi K and Biswal S 2021 *Soft Matter* **17** 1120
[22] Müller K, Osterman N, Babic D, Likos C, Dobnikar J and Nikoubashman A 2014 *Langmuir* **30** 5088
[23] Osterman N, Poberaj I, Dobnikar J, Frenkel D, Ziherl P and Babic D 2009 *Phys. Rev. Lett.* **103** 228301
[24] Tanaka F 2011 *Polymer Physics: Applications to Molecular Association and Thermoreversible Gelation* (Cambridge Univisity Press)
[25] Dickinson E 2014 *Annual Review of Food Science and Technology* **6** 211
[26] Kumar Nair P, Vasconcelos W, Paine K and Calabria-Holley J 2021 *Construction and Building Materials* **291** 123065
[27] Parente E, Ochoa Andrade A, Ares G, Russo F and Jimenez-Kairuz A 2015 *International Journal of Cosmetic Science* **37** 511
[28] Li C, Obireddy S R and Lai W F 2021 *Drug Delivery* **28** 1954
[29] Wang X, Ramírez-Hinestrosa S, Dobnikar J and Frenkel D 2019 *Phys. Chem. Chem. Phys.* **22** 10624
[30] Langevin P 1908 *Comptes rendus de l'Académie des Sciences* **146** 530
[31] Lemons D and Gythiel A 1997 *American Journal of Physics* **65** 1079
[32] Allen M P and Tildesley D J 1987 *Computer Simulation of Liquids* (Clarendon Press)
[33] Landau L and Lifshitz E 1987 *Fluid Mechanics* (2nd Edn.) **6** 505
[34] Han M, Fruchart M, Scheibner C, Vaikuntanathan S, de Pablo J and Vitelli V 2021 *Nat. Phys.* **17** 1260
[35] Weeks J D, Chandler D W and Andersen H C 1971 *Journal of Chemical Physics* **54** 5237
[36] Lees A and Edwards S 1972 *J. Phys. C: Solid State Phys.* **5** 1921
[37] Evans D J and Morriss G P 2008 *Statistical Mechanics of Nonequilibrium Liquids* (Cambridge University Press)
[38] Shang X and Leimkuhler B 2017 *Soft Matter* **13** 8565
[39] Nguyen H, Graham A, Koenig P and Gelb L 2020 *Soft Matter* **16** 256
[40] Whittle M and Dickinson E 1997 *Molecular Physics* **90** 739
[41] Heyes D M and Mitchell P J 1994 *Journal of the Chemical Society, Faraday Transactions* **90** 1931
[42] Irving J H and Kirkwood J G 1950 *J. Chem. Phys.* **18** 817
[43] Dolezal J and Jack R 2022 *Phys. Rev. Research* **4** 033134
[44] Chandler D 1987 *Introduction to Modern Statistical Mechanics* (Oxford University Press)
[45] Nelson D R and Halperin B I 1979 *Phys. Rev. B* **19** 2457
[46] Steinhardt P, Nelson D and Ronchetti M 1983 *Phys. Rev. B* **28** 784
[47] Mbamala E and von Gruenberg H 2003 *Phys. Rev. E* **67** 031608
[48] Ramasubramani V, Dice B D, Harper E S, Spellings M P, Anderson J A and Glotzer S C 2020 *Computer Physics Communications* **254** 107275
[49] Asakura S and Oosawa F 1954 *J. Chem. Phys.* **22** 1255
[50] Asakura S and Oosawa F 1958 *Journal of Polymer Science* **33** 183
[51] Vrij A 1976 *Pure and Applied Chemistry* **48** 471
[52] Lang P and Liu Y 2016 *Soft Matter at Aqueous Interfaces; Lecture Notes in Physics* **917** (Springer)
[53] Shikata T and Pearson D S 1994 *Journal of Rheology* **38** 601
[54] Shikata T, Niwa H S and Morishima Y 1998 *Journal of Rheology* **42** 765
[55] Mewis J and Wagner N J 2012 *Colloidal Suspension Rheology* (Cambridge University Press)
[56] Clark A H and Ross-Murphy S B 1987 *Biopolymers* (Springer Berlin Heidelberg) p. 57
[57] Nishinari K 2009 *Progress in Colloid and Polymer Science* **136** (Springer) p. 87
[58] Johnson R M, Schrag J L and Ferry J D 1970 *Polymer Journal* **1** 742
[59] Mitsuda Y, Osaki K, Schrag J L and Ferry J D 1973 *Polymer Journal* **4** 24
[60] Osaki K 1973 *Advances in Polymer Science* **12** (Springer-Verlag Berlin Heidelberg) p. 1
[61] Ferry J D 1979 *Macromolecular Chemistry* p. 299
[62] Zaccarelli E 2007 *J. Phys. Condens. Matter* **19** 323101
[63] Lin F J, Liao J J, Wu J C and Ai B Q 2022 *Chin. Phys. B* **31** 036401
[64] Lou X, Liu R, Chen K, Zhou X, Podgornik R and Yang M 2022 *Chin. Phys. B* **31** 044704